



Functional LSMO foams for magneto-caloric applications

Michael R. Koblischka¹ · Anjela Koblischka-Veneva¹ · Jörg Schmauch¹

Received: 4 March 2024 / Accepted: 25 May 2024
© The Author(s) 2024

Abstract

The ferromagnetic $\text{La}_{1-x}\text{Sr}_x\text{MnO}_3$ (LSMO) manganites are ideal materials for magneto-caloric applications due to their high Curie temperature. Here, we prepare open-cell, porous LSMO foams starting from a commercial polyurethane (PU) foam and commercial LSMO powder with $x = 0.3$. The cut PU foams are then covered by a slurry of LSMO powder mixed with PVA and water, and then, the foams are subjected to a heat-treatment with two steps at 600 °C (burn-off organic material) and 1200 °C (sintering/compacting). The resulting ceramic LSMO foams are then characterized by X-ray, SEM, electron backscatter diffraction (EBSD) orientation mapping and magnetic measurements. The foam sample consists of randomly-oriented LSMO grains with an average grain size of 188 nm, being distinctly smaller than bulk samples of the same composition, but considerably larger than LSMO nanowires prepared by electrospinning. The magnetic data reveal a high Curie temperature like the bulk samples, and an entropy change, $-\Delta S_M$ slightly higher than that of the bulk samples, which points to a strong influence of the LSMO grain size. Thus, the resulting LSMO foam material is well suited for magneto-caloric applications at room temperature.

Keywords LSMO · Manganites · Foam · Magneto-caloric materials · Magnetic refrigeration

1 Introduction

The perovskite-type manganites (generic formula $A_{1-x}B_x\text{MnO}_y$) offer several different functionalities, including the colossal magneto-resistance (CMR) [1], which is interesting for various sensor elements [2–5], and large magnetic entropy changes [6, 7] at the Curie temperature, T_C , being interesting e.g., for thermal storage as well as for magnetic refrigeration [8, 9]. For magnetic refrigeration using the magneto-caloric effect (MCE), the manganites have to compete with several types of metallic compounds, see e.g., the reviews by Gschneidner et al. [8], Gottschall et al. [10] and Belo et al. [11]. Now, it is obvious that the different functionalities may also require different shapes of the functional material to achieve optimum performance, i.e., thin films

and nanowires for magnetic sensor elements and bulks for magnetic refrigeration.

Bulk ceramic materials of perovskite-type manganites are polycrystalline materials, mechanically compacted (pressure $\approx 16 \text{ kN/cm}^2$) to form dense pellets with 70–85% theoretical density [12]. Thus, such materials are typically quite heavy, difficult to be shaped, etc. For the design of a magnetic refrigeration unit, the active material should have an amount of porosity, which can be reached by material processing (i.e., pores), but also by stacking platelets, ball-shaped samples, and other combinations [13, 14]. All such attempts require excessive work to obtain the final sample configuration.

A way out of these problems is given by employing porous bulk materials [15, 16]. The material aspects of such materials were recently reviewed in [17, 18]. Among these materials, the open-cell, ceramic foams, which can be prepared by using polyurethane (PU) open-cell foams as a base [19, 20], occupy a special place allowing an easy fabrication process of large samples as well as additional treatments like metallic underlayers [21] and additional coating of the final products. This may play an important role considering the chemical stability and corrosivity in the practical use of magneto-caloric materials [13]. The

✉ Michael R. Koblischka
m.koblischka@gmail.com

Anjela Koblischka-Veneva
a.koblischka@gmail.com

Jörg Schmauch
schmauch@nano.uni-saarland.de

¹ Experimental Physics, Saarland University, P.O.
Box 151150, 66041 Saarbrücken, Germany

porosity of the final material is defined by the PU foam employed, and the functional ceramic is to be prepared as powder with a given grain size, mixed up with an amount of PVA to form a slurry, where the PU foam is covered with [22–24]. After a final heat treatment to burn off the organic compounds and to sinter/compact the ceramic material, a functional ceramic foam can be obtained. The open-cell foam structure provides several advantages like optimized heat exchange (as the coolant can run through the sample itself), low sample weight and the possibility to straightforwardly upscale the sample size as well as to prepare a large variety of sample shapes, e.g., by cutting the PU foam material.

Such ceramic foams were already prepared as superconducting foams using the high- T_c superconducting (HTSc) material, $\text{YBa}_2\text{Cu}_3\text{O}_y$ (YBCO) [22–26]. With this type of foam, the excellent cooling efficiency could directly be demonstrated (see, e.g., the Supplementary Material of Ref. [27]). Thus, it is only straightforward to use the gained experience with the ceramic superconducting foams to prepare ceramic, thermoelectric or magnetocaloric foam materials as illustrated in Fig. 1. All these functionalities may profit from the foam-type material via improved heat exchange. A first step in this direction was already published by Salazar-Munoz et al. in [28], but adding the LSMO particles into the PU material itself.

For the magnetocaloric applications, we have chosen the compound $\text{La}_{1-x}\text{Sr}_x\text{MnO}_3$ (abbreviated: LSMO) with $x = 0.3$, which is the most interesting composition for near room-temperature refrigeration with its high T_C of 360 K. Employing various dopings, T_C can be increased up to 377 K [12, 29–32]. This material was already studied in different sample shapes in earlier publications, in form of electrospun, non-woven nanowire networks [33, 34] and as bulk samples [12]; thus, a direct comparison of the resulting properties becomes possible.

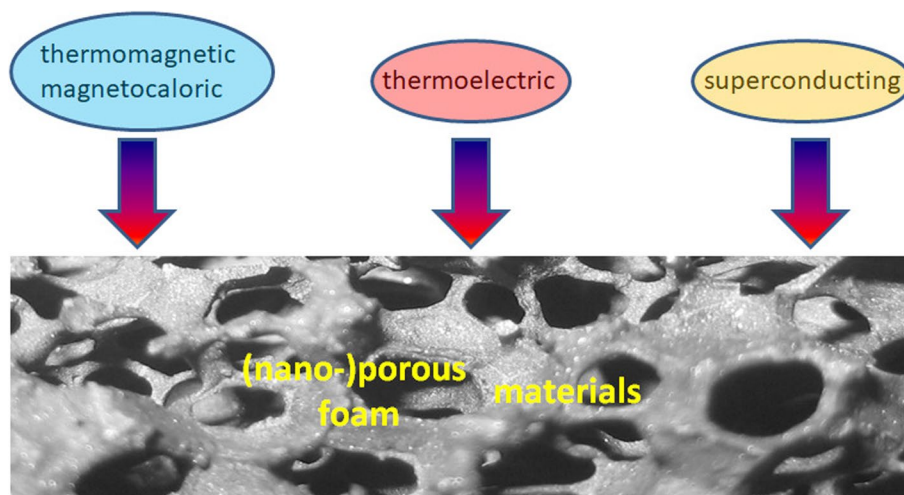
In this contribution, we present the fabrication of the first LSMO foams on the base of commercial PU foams, an analysis of the microstructure by SEM (EBSD) and magnetic measurements.

2 Experimental

Commercial LSMO powder of the type $\text{La}_{0.7}\text{Sr}_{0.3}\text{MnO}_{3-\delta}$ (Cerpotech Norway, LSM-73). This material was prepared using spray pyrolysis which gives a very fine, sub-micron, and high quality powder in terms of homogeneity and exact stoichiometry [35]. In the present experiment, small-sized foams ($10 \times 10 \times 10 \text{ mm}^3$) enabling magnetic measurements with the intact foam structure and larger ones ($20 \times 20 \times 30 \text{ mm}^3$) intended for demonstrators were cut from the large commercially available PU foam mats [36] prior to the coating. Batches of the LSMO powder were mixed with 2–5 wt% PVA as binder and water, the content of which in the slurry was adjusted to about 17–20% according to Ref. [24]. Furthermore, the slurry was stirred at $\sim 70^\circ\text{C}$ and maintained there before the coating [24]. Then, the foams were dipped into this slurry and dried at room temperature. This process was repeated up to 5 times in order to obtain a thick coating of the foam struts. The coated foams were then subjected to a heat treatment in a laboratory box furnace. In a first stage, the polymers are burnt away by slow heating at a rate of 50 K h^{-1} to 600°C and maintaining there for 6 h. The following step is the sintering/compacting of the LSMO material, which was performed at 1200°C (heating rate of 100 K h^{-1}) and held there for 20 h. Finally, the samples were cooled down to room temperature with a rate of 100 K h^{-1} .

For the microstructure analysis, foam strut pieces were broken out from the demonstrator-type foams according to [25]. Sample surfaces intended for EBSD analysis were treated by

Fig. 1 Scheme presenting several types of functional materials (thermomagnetic/magnetocaloric, thermoelectric and superconducting), where the (nano-)porous or foam structure may provide several interesting benefits for applications, mainly by an improved thermal exchange and weight/material reduction



mechanical polishing with various SiO₂ grinding papers, followed by mechanical polishing with diamond pastes (3 μm down to 1/4 μm diamonds) using ethanol as lubricant. As final step, the sample surface received a polishing treatment of the surface by colloidal silica with 40 nm particles (Struers OP-S solution) on the respective cloth. To clean up the surfaces, the samples were subjected to ultrasound cleaning in a solution of alcohol and acetone. More details on our sample surface preparation can be found in [37]. Low-angle (5°) Ar ion polishing (5 keV, 5 min) was eventually applied to the sample surface in order to enhance the resulting image quality (IQ) of the Kikuchi patterns. This step mainly removes adhered particles on the sample surface.

A Keyence VHX-5000 microscope [38] with large depth of field and long observation distance (most images were taken with 100× magnification) enabled to perform 3D imaging and digital image processing/analysis. The images were treated by the built-in analysis software for calibration and size measurements. Additional image analysis (e.g., for determining the powder grain size) was performed using ImageJ [39] and WSxM software [40]. Crystal structures were drawn using the VESTA software [41].

SEM images were taken using a field emission scanning electron microscope (JEOL 7600 F) and a JEOL 7000F SEM microscope operating at 20 kV with a working distance of 10 mm. For EDX analysis, an EDAX ZAF system with a SUTW sapphire detector was employed.

The EBSD orientation imaging was performed in a JEOL 7000F SEM microscope equipped with a TSL (TexSEM Labs, UT [42]) analysis unit. The Kikuchi patterns were generated in reflection mode at a voltage of 15 kV with a working distance of 20 mm, and recorded using a DigiView camera system. For the crystallographic orientation mapping, the electron beam was scanned over a selected surface area and the resulting Kikuchi patterns were captured, indexed and analyzed automatically by the controlling computer. Various such automated EBSD scans were carried out with step sizes down to 10 nm, which requires excellent surface quality (i.e., corresponding to high image quality (IQ) values).

Magnetic measurements were performed with a Quantum Design PPMS extraction magnetometer as well as a MPMS3 SQUID system (± 7 T maximum field) [43]. The magnetic field was applied perpendicular to the surface of the foam strut and the field sweep rate in the case of the SQUID system was 0.36 T/min.

3 Results and discussion

3.1 Microstructure

Figure 2 presents the X-ray and EDS data of the LSMO samples in different preparation stages. In Fig. 2a, the X-ray

data of the commercial LSM-73 powder are shown (this data set was provided by the manufacturer), together with the indexation analogous to (b). The data demonstrate the purity and homogeneity of the LSMO material as promised. In (b), the X-ray data of the as-prepared LSMO foam are shown in a wider 2 Θ -range. Also here, the material is chemically pure as no additional peaks appear after the heat processing treatment. The indexation was done using the JCPDS PDF-card #51-0409 for the composition La_{0.7}Sr_{0.3}MnO₃, assuming an rhombohedral crystal structure *Pnma* with $a = 5.459$ Å, $b = 5.568$ Å and $c = 7.709$ Å.

The X-ray line broadening of the reflections of (012), (104), (202), (024), (122), (214), (208) and (128) were employed to determine the average crystallite sizes of the LSMO foam struts. For this purpose, we used the Scherrer's equation

$$D = K\lambda/(\beta \cos \Theta), \quad (1)$$

where λ denotes the X-ray wavelength, K is a constant and was taken as 0.89, Θ gives the diffraction angle and β describes the full width at half maximum (FWHM) of each X-ray peak.

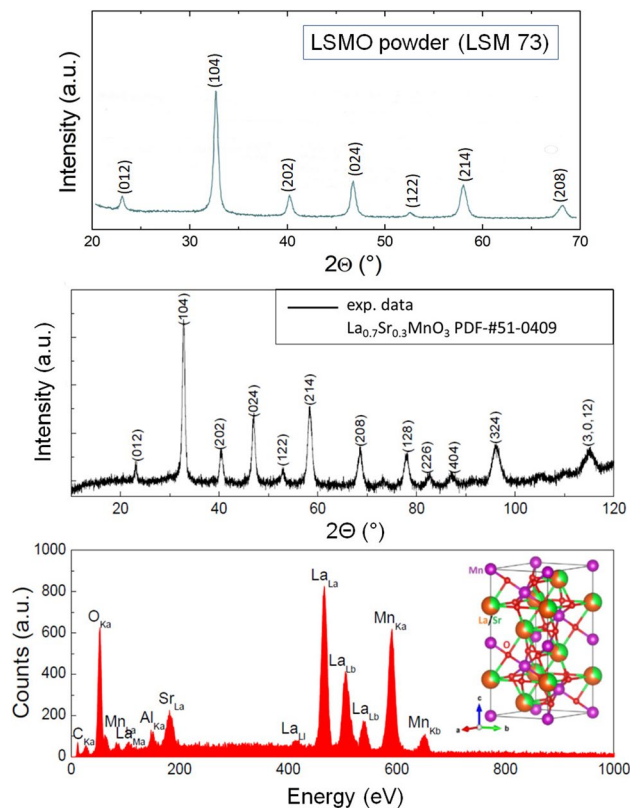


Fig. 2 X-ray and EDS analysis of LSMO. **a** Gives the data of the as-delivered LSM-73 powder. **b** Shows the x-ray data of the prepared LSMO foam (indexation of the peaks was done using the JCPDS-file #51-0409). **c** Presents the EDS analysis of an LSMO foam strut

Figure 3 presents SEM images of the commercial LSM-73 powder, enabling an analysis of the LSMO grain size. One can see that there are LSMO grains in form of platelets, partly stacked together. An optical analysis of several of these images using the software ImageJ reveals a mean grain size of 207 nm, which is considerably smaller than the bulk materials studied in [12], but significantly larger than that of the nanowires analyzed in [33, 34]. In order to create an uniform particle distribution, an ultrasound treatment analogous to the report in [44] will be useful, but was not tried for the first test samples prepared here.

Figure 4a–c provide SEM images of the prepared LSMO demonstrator foam. One can see the pore structure with open windows, which have sizes between 1 and 2 mm. Furthermore, some windows are closed which indicates that the slurry of LSMO powder, PVA and water could have been better optimized, which will be done in further experiments. The most important finding is here that the foam is consisting completely of LSMO, and the PU/PVA has completely burned off during the heat treatment. Using higher magnification (c), it gets obvious

that the foam struts look different to the superconducting foam materials prepared previously. The foam struts reveal directly signs of the various LSMO grains, so in this sense these LSMO foams are more similar to the Y_2BaCuO_5 (Y-211) foams prepared by Reddy et al. [24], which served as base material for the production of superconducting YBCO foams. In both cases, the foams consist of grains which were compacted together during the heat treatment with only minor changes of the grain size. In contrast, during the infiltration-growth processing applied for the preparation of YBCO foams, where a liquid phase has a capillary flow along the entire foam structure, the surfaces of the YBCO foam struts are altered and are much more homogeneous, showing also remnants of the material flow on them as described in [45]. The yellow circle in (c) marks a foam piece, which can be broken out for the detailed microstructure analysis by EBSD or for magnetic measurements, where a small-sized sample is required. Finally, (d) presents a digital, 3D-optic image obtained using the Keyence microscope and software. This image reveals the detailed structure of a foam window (similar to

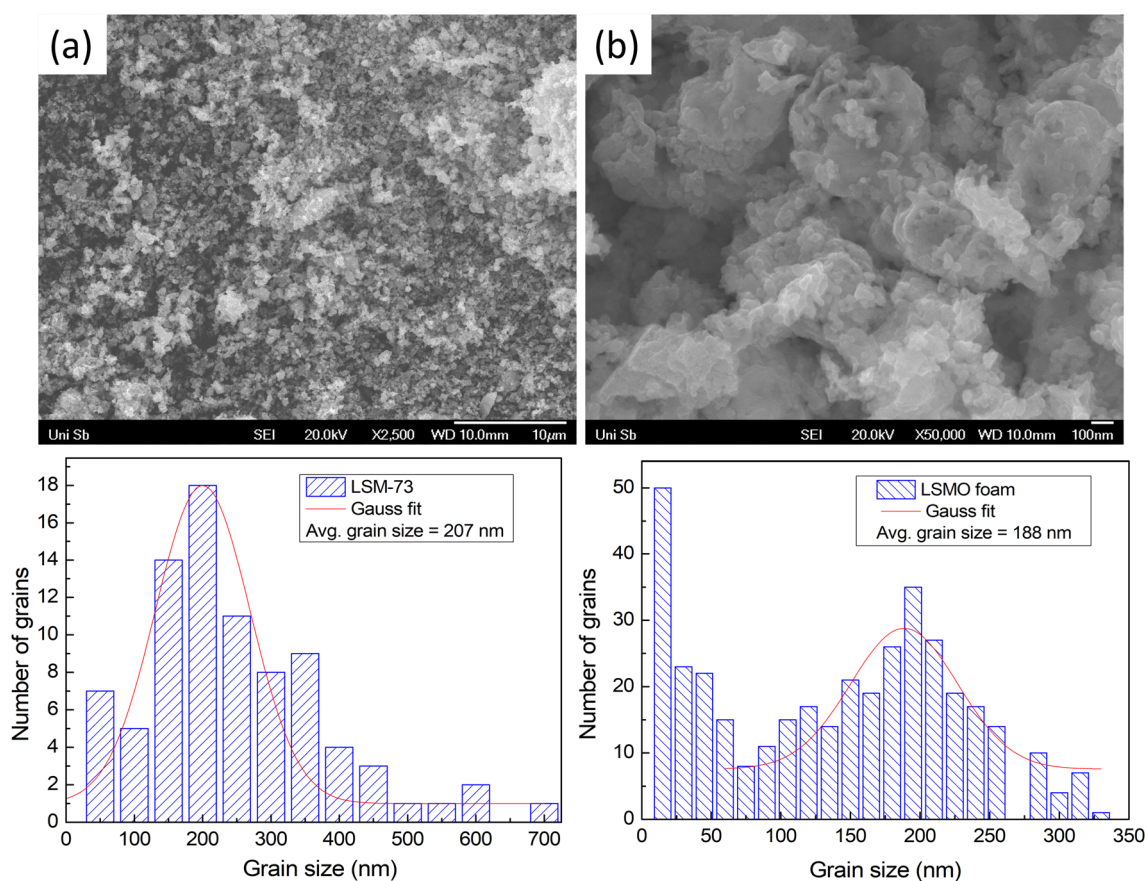


Fig. 3 a, b SEM images of the initial LSM-73 powder as obtained from the manufacturer. a Magnification 2500 \times , b 50,000 \times . From various images like (b), an optical grain size analysis was performed using ImageJ [39]. c Grain size histogram for the LSM-73 powder,

together with a Gauss fit. The average grain size is about 207 nm. d Grain size analysis from EBSD mappings of the LSMO foam, together with a Gauss fit, only considering grains larger than 50 nm. The average grain size determined is 188 nm

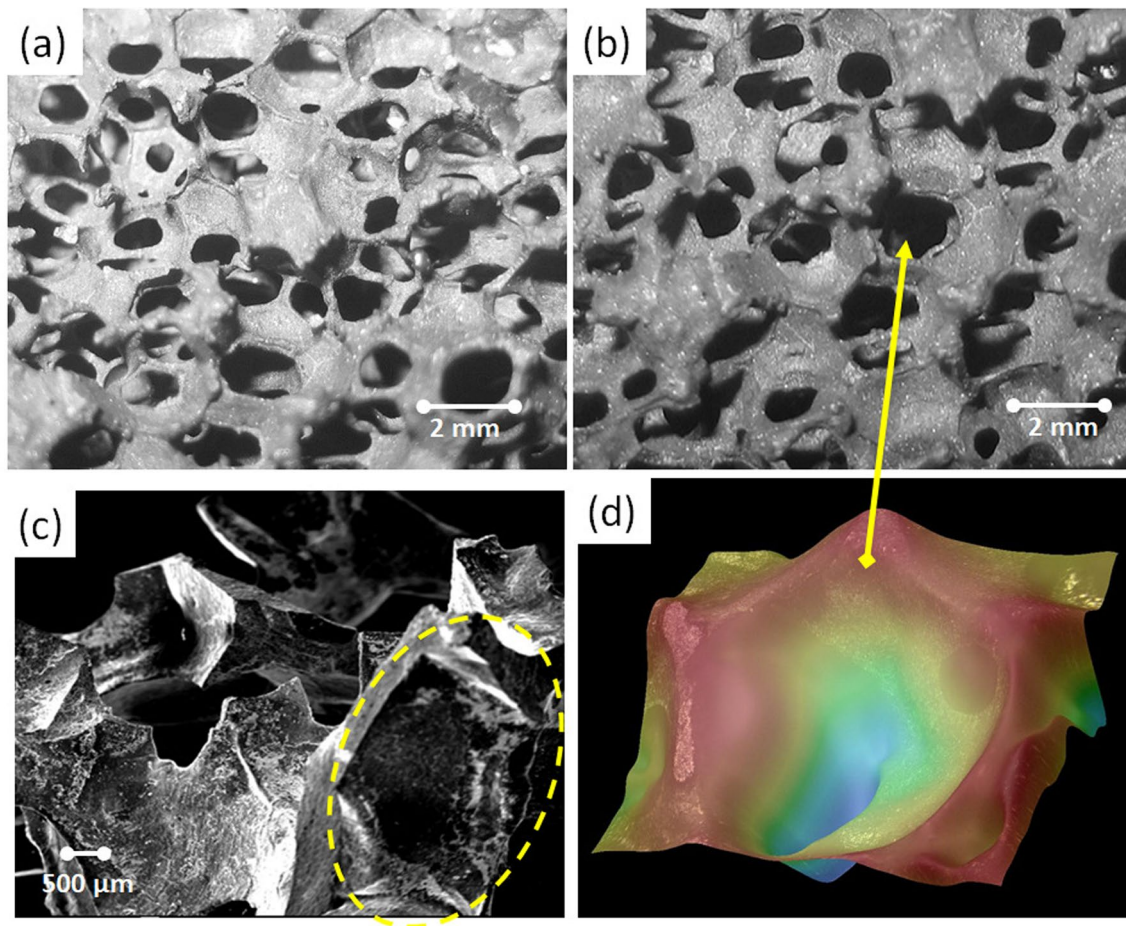


Fig. 4 **a, b** Two SEM images of the LSMO foam structure with low magnification revealing the arrangement of the foam windows, struts and ligaments. The figure reveals further that several windows are closed by LSMO material. **c** Presents broken-out pieces from the large foam with higher magnification. Pieces as the one marked

by the dashed-yellow circle) can be used for further analysis of the internal microstructure and for magnetic measurements. **d** Gives a 3D-optical image created using the Keyence digital microscope and software for analysis of the foam parameters

one as marked by a yellow arrow), allowing to extract the characteristic parameters according to Ref. [45].

In Fig. 5a–d, the results of EBSD orientation imaging are presented. For this analysis, a broken-out foam strut was employed as the sample surface must undergo a mechanical polishing procedure (see Sect. 2), which is not possible with a complete foam structure. The recorded EBSD Kikuchi patterns were indexed using the data set #470444 for LSMO with orthorhombic structure, but the *c*-axis length was adapted according to PDF-card #51-0409. Figure 5a presents an inverse pole figure (IPF) mapping in (001) direction, that is, perpendicular to the sample surface. This map (1000 × 1000 pixels, step size 10 nm, average IQ = 960) shows the grain orientations according to the stereographic triangle given below the figure. All the LSMO grains detected by EBSD are randomly oriented as visualized by the rainbow-like orientation colors, showing high-angle grain boundaries (GBs) between the LSMO

grains as indicated by black lines in Fig. 5a. A large number of high-angle GBs is obtained (2° – 5° : 12.9% with a total GB length of 3.04 μm, 5° – 15° : 1%, 15° – 180° : 86.2% with a total GB length of 20.3 μm). To ensure the validity of the results obtained, several such areas were mapped. Furthermore, there are no pores visible in the microstructure (i.e., all recorded Kikuchi patterns were indexed as LSMO) in this sample area which indicates that the PU/PVA was well burnt off during the heat treatment applied.

Figure 5b presents a grain size map in gray scale (300 nm = white, 5 nm = black). Furthermore, one can see several larger LSMO grains with sizes ranging between 100 and 300 nm, but also a large amount of tiny LSMO grains with dimensions around 10–20 nm. Figure 5c presents the inverse pole figure corresponding to the mapping of (a), again indicating the random arrangement of the LSMO grains. In total 5 such areas were mapped and the evaluated grain size distribution is shown in Fig. 3d. Finally, Fig. 5d

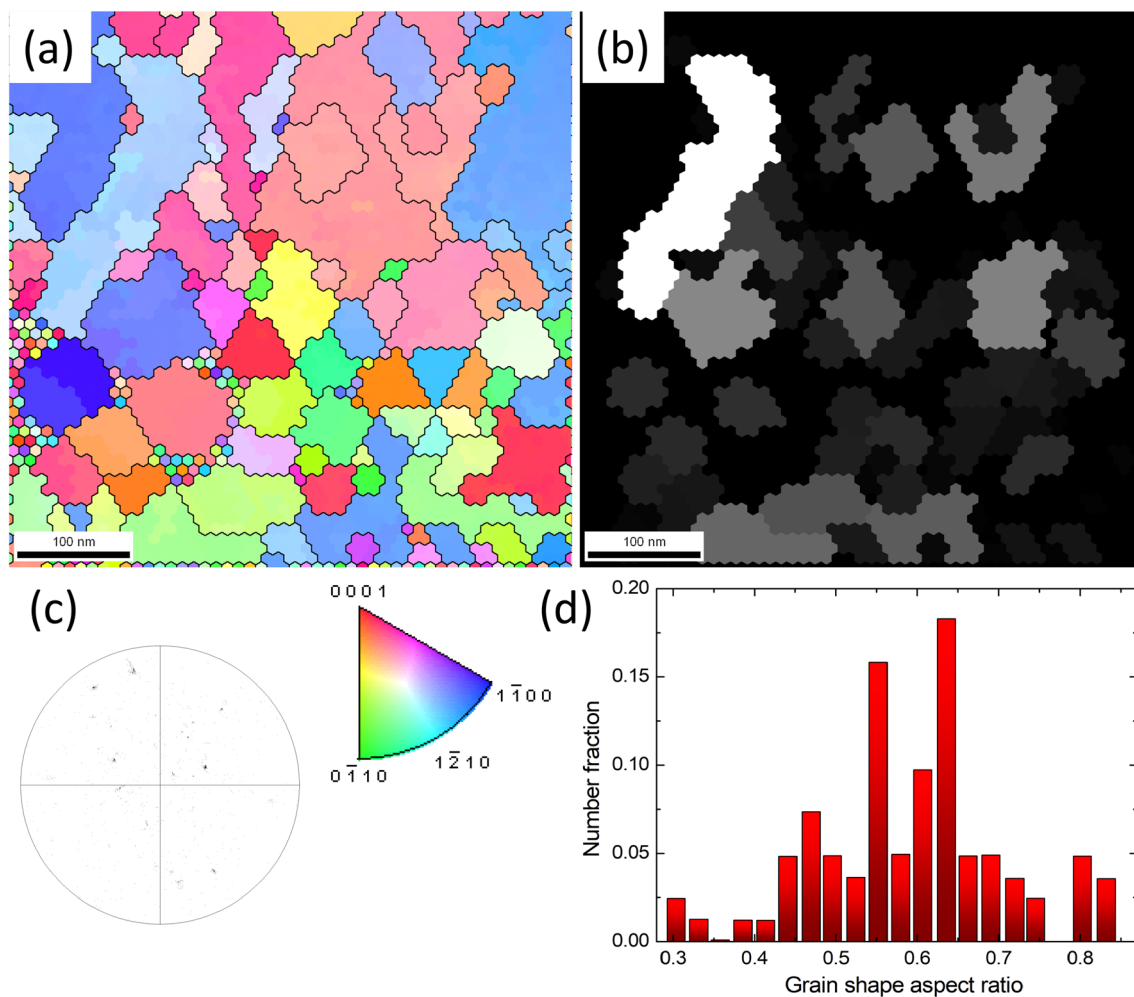


Fig. 5 a–c EBSD orientation imaging. **a** is an inverse pole figure map (1000×1000 pixels, step size 10 nm) in (001) orientation (perpendicular to the sample surface) with the EBSD-detected GBs marked by black lines. The color code for the grain orientations is given below the map. **b** Represents a grain size mapping of the same area

in gray scale (300 nm = white, 5 nm = black). **c** Shows the discrete pole figure in (001)-direction, indicating the random orientation of the LSMO grains. **d** is a grain shape aspect ratio plot (for details, see the main text)

presents an analysis of the grain shape aspect ratio, which gives interesting extra information concerning the grain growth. To obtain this ratio, the software places ellipses (long axis a , short axis b) on the detected grains, and the obtained axis lengths are then analyzed via the relation $g_{ar} = b/a$. The resulting g_{ar} ranges between 0 and 1, with 1 indicating $a = b$. From the graph one can see that the larger LSMO grains are represented by elongated ellipses. Two large maxima in the graph are obtained at 0.55 and 0.65, which indicates that about 30% of the grains are slightly elongated. Overall, the grain shape aspect ratio distribution found here is similar to the one of the LSMO nanowires of Ref. [46], however, the present foam sample reveals the presence of several large and very elongated LSMO grains, which did not appear in the case of the LSMO nanowire networks.

3.2 Magnetization data

For these measurements, broken-out foam struts from a demonstrator-type foam sample were used due to the sample space limitations of the QD extraction magnetometer employed.

In Fig. 6a, b, the magnetization M is shown as function of temperature in the range $150 \text{ K} \leq T \leq 400 \text{ K}$ for an applied magnetic field of 0.05 T (a) and 2 T (b). The data for the LSMO foam are highlighted in orange (●). For comparison, this plot presents the data of Ref. [12] for the same LSMO composition with $x = 0.3$ (●) and two other compositions, $\text{La}_{0.67}\text{Ca}_{0.33}\text{MnO}_3$ (LCMO, ▼) and $\text{La}_{0.67}\text{Ba}_{0.33}\text{MnO}_3$ (LBMO, ▲). For both LSMO samples, the transition is not yet completed at $T = 400 \text{ K}$ (the maximum temperature realized in the equipment), when a magnetic

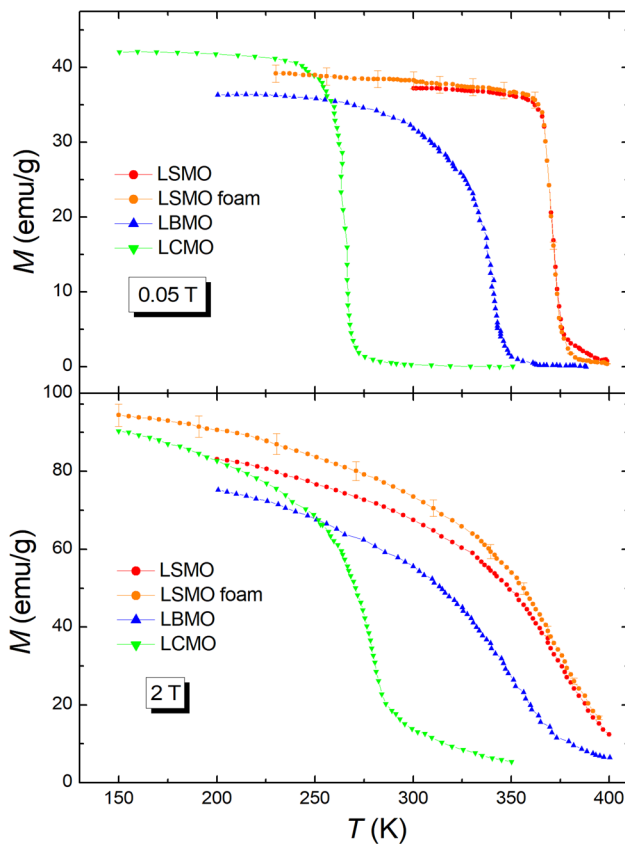


Fig. 6 **a** Magnetization M versus temperature, T at $\mu_0 H = 0.05$ T for the LSMO foam (●) in the temperature range $150 \text{ K} \leq T \leq 400 \text{ K}$ and bulk materials of LSMO (●), LCMO (▼) and LBMO (▲) from Ref. [12] for comparison. The error bars indicate the variation of M recorded for different LSMO foam struts. **b** M vs. T at an applied magnetic field of $\mu_0 H = 2$ T for the same materials

field of 2 T was applied. Here, one can see the outstanding position of LSMO with the highest Curie temperatures, whereas LCMO reveals a much steeper transition, which led consequently to a larger ΔS_M -value [12]. One must note also that the LSMO foam data at 0.05 T are very similar to those of the bulk LSMO sample studied previously, but at lower temperatures, the obtained magnetization is somewhat higher for the LSMO foam. At 2 T applied magnetic field, the data for the LSMO foam are found to be always higher than the corresponding bulk material. The error bars indicate the variation of the magnetization of about 3% found for different foam struts, broken-out of various locations in the original foam sample. In Ref. [25], we had found a strong variation of the superconducting properties with the positions of the struts in the original bulk foam sample, which is clearly not the case here. This points to effects of the infiltration growth technique, which is applied in the preparation of the YBCO foams, but not required for the LSMO samples.

The magnetic entropy change $-\Delta S_M$ is given by [47–49]

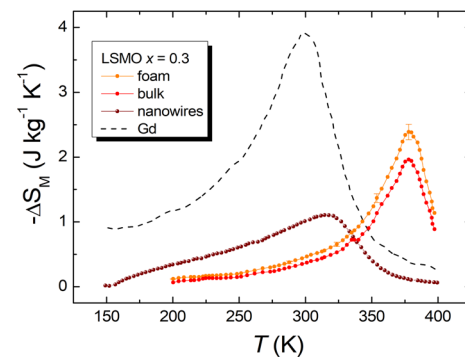


Fig. 7 $-\Delta S_M$ versus temperature with $\delta(\mu_0 H) = 2$ T. All data are for various LSMO samples with $x = 0.3$, i.e., LSMO foam (●), LSMO bulk (●) and LSMO nanowire networks (●). The error bars on the LSMO foam data indicate the experimental variation when employing different foam struts. For comparison, the data for metallic Gd (— — —) of Ref. [12] are shown as well

$$\Delta S_M = \mu_0 \int_0^H \left[\frac{\delta M}{\delta T} \right]_H dH. \quad (2)$$

For magnetization measurements performed at discrete fields and temperature intervals, ΔS_M can be approximated by writing [47–49]

$$|\Delta S_M| = \sum \Delta H_i \frac{(M_i - M_{i+1})_H}{(T_{i+1} - T_i)}, \quad (3)$$

where M_i and M_{i+1} are the magnetization values measured at a field H and at temperatures T_i and T_{i+1} , respectively. Finally, the relative cooling power (RCP) can be expressed as

$$\text{RCP} = |\Delta S_M^{\max}| \cdot \delta T_{\text{FWHM}}, \quad (4)$$

with ΔS_M^{\max} denoting the maximum of the entropy change, and δT_{FWHM} is the width of the peak at half maximum.

Figure 7 presents the calculated $-\Delta S_M$ for three different types of LSMO material with $x = 0.3$. The LSMO foam is again given as (●), the bulk LSMO as (●). For comparison, data of LSMO nanowires (see, e.g., Ref. [34]) are given in dark red (●). The data for the LSMO-foam and the -bulk are quite similar to each other, with the foam data being always higher in the entire temperature range. This is valid also when considering the variation (error bars) caused by foam struts broken out of different locations in the original foam. The maximum of the peak is found at the same temperature (378 K) and with nearly the same peak width, but $|\Delta S_M^{\max}|$ is different, i.e., $1.96 \text{ J kg}^{-1} \text{ K}^{-1}$ (LSMO bulk) and $2.4 \text{ J kg}^{-1} \text{ K}^{-1}$ (LSMO foam). Remarkably, the data of the LSMO nanowire network show a completely different behavior as compared to the two bulks: The peak in $-\Delta S_M(T)$ is found to be extremely broad, yielding $|\Delta S_M(\text{nanowire})| > |\Delta S_M(\text{bulks})|$ in the temperature range 200–325 K. The corresponding

peak height located at 316.6 K is, however, much smaller with $|\Delta S_M^{\max}| = 1.07 \text{ kg}^{-1} \text{ K}^{-1}$. The data of metallic Gd from Ref. [12] reveal that all recorded peak temperatures for the LSMO compounds are well above 300 K and above the peak temperature of Gd. As the 3 LSMO compounds differ mainly in their grain sizes, this graph demonstrates the grain size of the material has a strong influence on the resulting $|\Delta S_M(T)|$.

The calculation of RCP yields 112.8 J kg^{-1} for the LSMO foam and 88.2 J kg^{-1} for the LSMO bulk, being well in the range as shown in Refs. [6, 7, 50, 51] and can be well compared to various metallic materials [52], but at higher temperatures well above room-temperature. Very remarkable is, however, the RCP value for the LSMO nanowire network with 111.2 J kg^{-1} , which is due to the very broad peak in $|\Delta S_M(T)|$. The clarification of this issue will be a topic of subsequent work.

Regarding the data obtained for the LSMO foam, it is clearly demonstrated that the achieved LSMO grain size in the 100-nm range is beneficial for the resulting $|\Delta S_M(T)|$. Future experiments will try to optimize the preparation conditions further, especially the viscosity of the coating slurry as well as the applied temperature treatment. Via ultrasound treatment of the starting powder material, the LSMO grain size may further be optimized as well.

4 Conclusion

So, let us summarize here the present investigation. Open-cell, porous LSMO foams with $x = 0.3$ were prepared on the base of commercially available PU foams and commercial LSMO powder. The microstructure analysis revealed that these foams consist of randomly-oriented LSMO grains with an average grain size of 188 nm, which is much larger compared to LSMO nanowire networks, but smaller than that of typical LSMO bulks. The grain size obtained for the LSMO foams leads to a higher entropy change, $-\Delta S_M$, and a higher RCP value as compared to the bulk LSMO samples, which is a promising result for the development of LSMO foam materials for magnetic cooling.

Acknowledgements We thank X.L. Zeng (Saarland University) for providing the data of the entropy change of the LSMO nanowire networks. Part of this work was supported by the SUPERFOAM international project funded by ANR and DFG under the references ANR-17-CE05-0030 and DFG-ANR Ko2323-10, which is gratefully acknowledged.

Author Contributions M.R. Koblichka: conceptualization, methodology, validation, formal analysis, investigation, writing—review and editing, visualization, project administration. A. Koblichka-Veneva: conceptualization, validation, formal analysis, investigation, writing—review and editing, visualization. Jörg Schmauch: formal analysis, investigation, writing—review and editing.

Funding Open Access funding enabled and organized by Projekt DEAL.

Data availability The data that support the findings of this study are available from the corresponding authors upon reasonable request.

Declarations

Conflict of interest The authors declare that they have no conflict of interest.

Open Access This article is licensed under a Creative Commons Attribution 4.0 International License, which permits use, sharing, adaptation, distribution and reproduction in any medium or format, as long as you give appropriate credit to the original author(s) and the source, provide a link to the Creative Commons licence, and indicate if changes were made. The images or other third party material in this article are included in the article's Creative Commons licence, unless indicated otherwise in a credit line to the material. If material is not included in the article's Creative Commons licence and your intended use is not permitted by statutory regulation or exceeds the permitted use, you will need to obtain permission directly from the copyright holder. To view a copy of this licence, visit <http://creativecommons.org/licenses/by/4.0/>.

References

1. A.P. Ramirez, Colossal magnetoresistance. *J. Phys.: Condens. Matter* **9**, 8171–8199 (1997)
2. M.G. Kang, H.B. Kang, M. Clavel, D. Maurya, S. Gollapudi, M. Hudait, M. Sanghadasa, S. Priya, Magnetic field sensing by exploiting giant nonstrain-mediated magnetodielectric response in epitaxial composites. *Nano Lett.* **18**, 2835–2843 (2018). <https://doi.org/10.1021/acs.nanolett.7b05248>
3. M. Enhessari, A. Salehabadi, Perovskites-based nanomaterials for chemical sensors, in *Progresses in Chemical Sensor*. ed. by W. Wang (InTech, London, 2016). <https://doi.org/10.5772/62559>
4. V. Stankevicius, N. Zurauskienė, S. Kersulis, V. Plausinaitienė, R. Lukose, J. Klimantavicius, S. Tolvaišienė, M. Skapas, A. Selskis, S. Balevicius, Nanostructured manganite films grown by pulsed injection MOCVD: tuning low- and high-field magnetoresistive properties for sensors applications. *Sensors* **22**, 605 (2022). <https://doi.org/10.3390/s22020605>
5. L. Enger, S. Flament, I. Bhatti, O. Rousseau, B. Guillet, M.L.C. Sing, V. Pierron, S. Lebarry, S.K. Chaluvadi, B. Domengés, A. Vera, J.M. Díez, I. Martínez, R. Guerrero, L. Pérez, M.T. Gonzalez, R. Miranda, J. Camarero, P. Perna, L. Méchin, Key parameters for detectivity improvement of low noise anisotropic magnetoresistive sensors made of $\text{La}_{2/3}\text{Sr}_{1/3}\text{MnO}_3$ single layers on vicinal substrates. *ACS Appl. Electron. Mater.* **5**(2), 729–739 (2023). <https://doi.org/10.1021/acsaem.2c01096>
6. M.H. Phan, T.L. Phan, S.C. Yu, K.W. Lee, S.H. Park, Large magnetic entropy change above 300 K in manganites. *J. Korean Phys. Soc.* **45**, 664–667 (2004)
7. P.R. Nadig, M.S. Murari, M.D. Daivajna, Influence of heat sintering on the physical properties of bulk $\text{La}_{0.67}\text{Ca}_{0.33}\text{MnO}_3$ perovskite manganite: role of oxygen in tuning the magnetocaloric response. *Phys. Chem. Chem. Phys.* **26**, 5237 (2024). <https://doi.org/10.1039/d3cp04185a>
8. K.A. Gschneidner Jr., V.K. Pecharsky, A.O. Tsokol, Recent developments in magnetocaloric materials. *Rep. Prog. Phys.* **68**, 1479–1539 (2005). <https://doi.org/10.1088/0034-4885/68/6/R04>

9. O. Tegus, E. Brück, K.H.J. Buschow, F.R. de Boer, Transition-metal-based magnetic refrigerants for room-temperature applications. *Nature* **415**, 150–152 (2002)
10. T. Gottschall, K.P. Skokov, M. Fries, A. Taubel, I. Radulov, F. Scheibel, D. Benke, S. Riegg, O. Gutfleisch, Making a cool choice: the materials library of magnetic refrigeration. *Adv. Energy Mater.* **9**, 1901322 (2019). <https://doi.org/10.1002/aeem.201901322>
11. J.H. Belo, A.L. Pires, J.P. Araújo, A.M. Pereira, Magnetocaloric materials: from micro- to nanoscale. *J. Mater. Res.* (2019). <https://doi.org/10.1557/jmr.2018.352>
12. Y. Xu, M. Meier, P. Das, M.R. Koblischka, U. Hartmann, Perovskite manganites: potential materials for magnetic cooling at or near room temperature. *Cryst. Eng.* **5**, 383–389 (2002). [https://doi.org/10.1016/S1463-0184\(02\)00049-7](https://doi.org/10.1016/S1463-0184(02)00049-7)
13. S. Wojcieszak, B. Wodajo, A. Duong, R.L. Hdaimani, R. Barua, A brief review on the chemical stability and corrosivity of magnetocaloric materials. *JOM* **74**, 4368–4378 (2022). <https://doi.org/10.1007/s11837-022-05495-7>
14. A. Kitanovski, P.W. Egloff, Innovative ideas for future research on magnetocaloric technologies. *Int. J. Refrig.* **33**, 449–464 (2010). <https://doi.org/10.1016/j.ijrefrig.2009.11.005>
15. I. Nettleship, Applications of porous ceramics. *Key Eng. Mater.* **122–124**, 305–324 (1996). <https://doi.org/10.4028/www.scientific.net/KEM.122-124.305>
16. A. Sarlah, A. Kitanovski, A. Poredos, P.W. Egolf, O. Sari, F. Gendre, Ch. Besson, Static and rotating active magnetic regenerators with porous heat exchangers for magnetic cooling. *Int. J. Refrig.* **29**, 1332–1339 (2006). <https://doi.org/10.1016/j.ijrefrig.2006.07.013>
17. M.R. Koblischka, A. Koblischka-Veneva, Porous high- T_c superconductors and their applications. *AIMS Mater. Sci.* **5**, 1199–1213 (2018). <https://doi.org/10.3934/mat.2018.6.1199>
18. D. Gokhfeld, M.R. Koblischka, A. Koblischka-Veneva, ВЫСОКОПОРИСТЫЕ СВЕРХПРОВОДНИКИ: СИНТЕЗ, ИССЛЕДОВАНИЯ И ПЕРСПЕКТИВЫ. *Fizika Metalov i Metalovidenie* **121**, 1026–1038 (2020) (in Russian); D. Gokhfeld, M.R. Koblischka, A. Koblischka-Veneva, Highly porous superconductors: synthesis, research, and prospects. *Phys. Met. Metallogr.* **121**, 936–948 (2020) (English translation). <https://doi.org/10.1134/S0031918X20100051>
19. J. Banhart, Manufacture, characterisation and application of cellular metals and metal foams. *Prog. Mater. Sci.* **46**, 559–632 (2001). [https://doi.org/10.1016/S0079-6425\(00\)00002-5](https://doi.org/10.1016/S0079-6425(00)00002-5)
20. L.-P. Lefebvre, J. Banhart, D.C. Dunand, Porous metals and metallic foams: current status and recent developments. *Adv. Eng. Mater.* **10**, 775–787 (2008). <https://doi.org/10.1002/adem.20080241>
21. A. Jung, H. Natter, S. Diebels, E. Lach, R. Hempelmann, Nanonickel coated aluminum foam for enhanced impact energy absorption. *Adv. Eng. Mater.* **13**, 23–28 (2011). <https://doi.org/10.1002/adem.201000190>
22. E.S. Reddy, G.J. Schmitz, Superconducting foams. *Supercond. Sci. Technol.* **15**, L21–L24 (2002). <https://doi.org/10.1088/0953-2048/15/8/101>
23. E.S. Reddy, G.J. Schmitz, Ceramic foams. *Am. Ceram. Soc. Bull.* **81**, 35–37 (2002)
24. E.S. Reddy, M. Herweg, G.J. Schmitz, Processing of Y_2BaCuO_5 foams. *Supercond. Sci. Technol.* **16**, 608–612 (2003). <https://doi.org/10.1088/0953-2048/16/5/311>
25. M.R. Koblischka, A. Koblischka-Veneva, K. Berger, Q. Nouailhetas, B. Douine, E.S. Reddy, G.J. Schmitz, Current flow and flux pinning properties of YBCO foam struts. *IEEE Trans. Appl. Supercond.* **29**, 8001405 (2019). <https://doi.org/10.1109/TASC.2019.2894712>
26. M.R. Koblischka, A. Koblischka-Veneva, C. Chang, T. Hauet, E.S. Reddy, G.J. Schmitz, Flux pinning analysis of superconducting YBCO foam struts. *IEEE Trans. Appl. Supercond.* **29**, 8001905 (2019). <https://doi.org/10.1109/TASC.2018.2880334>
27. M.R. Koblischka, S. Pavan Kumar Naik, A. Koblischka-Veneva, M. Murakami, D. Gokhfeld, E.S. Reddy, G.J. Schmitz, Superconducting YBCO foams as trapped field magnets. *Materials* **12**, 853 (2019). <https://doi.org/10.3390/ma12060853>
28. V.E. Salazar-Muñoz, S.A. Palomares-Sánchez, I. Betancourt, A.A. Torres-Castillo, J.G. Cabal Velarde, A.L. Guerrero, Magnetic and magnetocaloric properties of a foam composite based on substituted La-manganite in a polyurethane matrix. *J. Magn. Magn. Mat.* **538**, 168296 (2021). <https://doi.org/10.1016/j.jmmm.2021.168296>
29. E.L. Hernández-González, S.A. Palomares-Sánchez, J.T. Elizalde Galindo, M. Mirabal-García, Magnetocaloric effect near room temperature of $La_{0.67}Ca_{0.33-x}Sr_xMnO_3$ ($x = 0.06, 0.07, 0.08$) manganites. *J. Supercond. Nov. Magn.* **28**, 1635–1638 (2015). <https://doi.org/10.1007/s10948-014-2932-2>
30. S. Biswas, S. Keshri, Large magnetocaloric effect near room temperature in $La_{0.67}(Sr,K/Pb)_{0.33}MnO_3$ manganite nanomaterials. *J. Mater. Sci.: Mater. Electron.* **31**, 21896–21912 (2020). <https://doi.org/10.1007/s10854-020-04694-9>
31. A.O. Ayas, S. Kılıç Çetin, G. Akça, M. Akyol, A. Ekicibil, Magnetic refrigeration: current progress in magnetocaloric properties of perovskite manganite materials. *Mater. Today Commun.* **35**, 105988 (2023). <https://doi.org/10.1016/j.mtcomm.2023.105988>
32. V.E. Salazar-Muñoz, A.L. Guerrero, S.A. Palomares-Sánchez, Review of magnetocaloric properties in lanthanum manganites. *J. Magn. Magn. Mater.* **562**, 169787 (2022). <https://doi.org/10.1016/j.jmmm.2022.169787>
33. X.L. Zeng, T. Karwoth, A. Koblischka-Veneva, M.R. Koblischka, J. Schmauch, U. Hartmann, T. Hauet, Magnetoresistance and structural characterization of electrospun $La_{1-x}Sr_xMnO_3$ nanowire networks, in *Nanowires—Synthesis, Properties and Applications*, Chap. 6. ed. by S. Rackauskas (Intechopen, London, 2019). <https://doi.org/10.5772/intechopen.80451>
34. T. Karwoth, X.L. Zeng, M.R. Koblischka, U. Hartmann, C. Chang, T. Hauet, J.-M. Li, Magnetoresistance and structural characterization of electrospun $La_{1-x}Sr_xMnO_3$ nanowire network fabrics with $x = 0.2$. *Solid State Commun.* **290**, 37–41 (2019). <https://doi.org/10.1016/j.ssc.2018.12.015>
35. Ceramic Powder Technology AS (Cerpotech), Kvenildmyra 6, N-7093 Tiller, Norway. <https://www.cerpotech.com/>. Accessed 14 Feb 2024
36. Filteron AG, Solingen, Germany. Available online: https://filteron.de/produkte/filterschaum_ppi. Accessed 14 Feb 2024
37. M.R. Koblischka, A. Koblischka-Veneva, Applications of the electron backscatter diffraction technique to ceramic materials. *Phase Trans.* **86**, 651–660 (2013). <https://doi.org/10.1080/01411594.2012.726729>
38. Keyence Corp. Digital optical microscopes. <https://www.keyence.com/products/microscope/digital-microscope/vhx-7000/>. Accessed 14 Feb 2024
39. Image J. Image processing and analysis in Java. <https://imagej.nih.gov/ij/index.html>. Accessed 14 Feb 2024
40. I. Horcas, R. Fernández, J.M. Gómez-Rodríguez, J. Colchero, J. Gómez-Herrero, A.M. Baro, WSXM: a software for scanning probe microscopy and a tool for nanotechnology. *Rev. Sci. Instrum.* **78**, 013705 (2007). <https://doi.org/10.1063/1.2432410>
41. K. Momma, F. Izumi, VESTA 3 for three-dimensional visualization of crystal, volumetric and morphology data. *J. Appl. Crystallogr.* **44**, 1272–1276 (2011)
42. TexSEM Laboratories (TSL) Orientation Imaging Microscopy Software V7.2, User Manual, TexSEM laboratories (TSL), Draper, UT, USA (2015).

43. Quantum Design, San Diego, CA. <https://qdusa.com/>. Accessed 14 Feb 2024
44. S.P.K. Naik, R. Hagiwara, S. Ishibashi, N. Asano, H. Ogino, S. Ishida, M.R. Koblischka, A. Koblischka-Veneva, Y. Tsuchiya, K. Kawashima, H. Eisaki, T. Nishio, Investigation of high-energy ultrasonication of $\text{RE}_2\text{BaCuO}_5$ (RE = Y, Gd) on the growth and superconducting properties of $\text{REBa}_2\text{Cu}_3\text{O}_{7-\delta}$ top-seeded melt textured bulks. *Supercond. Sci. Technol.* **35**, 074003 (2022). <https://doi.org/10.1088/1361-6668/ac6f8b>
45. M.R. Koblischka, A. Koblischka-Veneva, Q. Nouailhetas, G. Hajiri, K. Berger, B. Douine, D. Gokhfeld, Microstructural parameters for modelling of superconducting foams. *Materials* **15**, 2303 (2022). <https://doi.org/10.3390/ma15062303>
46. A. Koblischka-Veneva, M.R. Koblischka, X.L. Zeng, J. Schmauch, Microstructure analysis of electrospun $\text{La}_{0.8}\text{Sr}_{0.2}\text{MnO}_3$ nanowires using electron microscopy and electron backscatter diffraction (EBSD). *AIP Adv.* **11**, 025008 (2021). <https://doi.org/10.1063/9.0000171>
47. M. Földeaki, R. Chahine, T.K. Bose, Magnetic measurements: a powerful tool in magnetic refrigerator design. *J. Appl. Phys.* **77**, 3528–3537 (1995). <https://doi.org/10.1063/1.358648>
48. M.A. Hamad, Theoretical work on magnetocaloric effect in $\text{La}_{0.75}\text{Ca}_{0.25}\text{MnO}_3$. *J. Adv. Ceram.* **1**, 290–295 (2012). <https://doi.org/10.1007/s40145-012-0027-8>
49. M.A. Hamad, Theoretical work on effect of pressure on magnetocaloric properties of $\text{La}_{0.7}\text{Ca}_{0.3}\text{MnO}_3$. *Int. J. Thermophys.* **36**, 2748–2754 (2015). <https://doi.org/10.1007/s10765-015-1960-x>
50. L.H. Omari, A. Lekdadri, E.K. Hlil, H. Lassri, R. Moubah, A. Tozri, E. Dhahri, M. Kerouad, A. Zaim, Nano-sized magnetocaloric compounds investigation by using magnetization measurement and Monte Carlo simulation: case of LSMO nanoparticles. *Mater. Today Commun.* **23**, 100857 (2020). <https://doi.org/10.1016/j.mtcomm.2019.100857>
51. V. Anwar, S. Kumar, F. Ahmed, N. Arshi, G.W. Kim, B.H. Koo, Above room temperature magnetic transition and magnetocaloric effect in $\text{La}_{0.66}\text{Sr}_{0.34}\text{MnO}_3$. *J. Korean Phys. Soc.* **60**, 1587–1592 (2012). <https://doi.org/10.3938/jkps.60.1587>
52. L.D. Griffith, X. Mudryk, J. Slaughter, V.K. Pecharsky, Material-based figure of merit for caloric materials. *J. Appl. Phys.* **123**, 034902 (2018). <https://doi.org/10.1063/1.5004173>

Publisher's Note Springer Nature remains neutral with regard to jurisdictional claims in published maps and institutional affiliations.